A Machine Learning-Driven Solution for Denoising Inertial Confinement Fusion Images

Asya Y. Akkus, Bradley T. Wolfe, Pinghan Chu, Chengkun Huang, Chris S. Campbell, Mariana Alvarado Alvarez, Petr Volegov, David Fittinghoff, Robert Reinovsky, Zhehui Wang

Abstract-Neutron imaging is important in optimizing analysis of inertial confinement fusion (ICF) events such as those at the National Ignition Facility (NIF) and improving current and future ICF platforms. However, images of neutron sources are often degraded by various types of noise. Most commonly, Gaussian and Poisson noise often coexist within one image, obscuring fine details and blurring edges. These noise types often overlap, making them difficult to distinguish and remove using conventional filtering and thresholding methods. As a result, noise removal techniques that preserve image fidelity are important for analyzing and interpreting images of a neutron source. Current solutions include a combination of filtering and thresholding methodologies. In the past, machine learning approaches were rarely implemented due to a lack of ground truth neutron imaging data for ICF processes. However, recent advances in synthetic data production, particularly in the fusion imaging field, have opened opportunities to investigate new denoising procedures using both supervised and unsupervised machine learning methods. In this study, we implement an unsupervised autoencoder with a Cohen-Daubechies-Feauveau (CDF 97) wavelet transform in the latent space for mixed Gaussian-Poisson denoising. The network successfully denoises neutron imaging data. Additionally, it demonstrates lower reconstruction error and superior edge preservation metrics when benchmarked with generated by a forward model and compared to non-MLbased filtering mechanisms such as Block-matching and 3D filtering (BM3D). This approach presents a promising advancement in neutron image noise reduction and threedimensional reconstruction analysis of ICF experiments.

Index Terms—Plasma diagnostics, Image processing, Machine learning, Image filtering, Gaussian noise, Unsupervised Learning, Neutrons, Laser Fusion

I. INTRODUCTION

ONFINEMENT fusion is the process of inducing fusion of atomic nuclei under high temperature and pressure in a confined space with the goal of achieving and replicating fusion breakeven and ultimately energy gain [1]. As a result, diagnostics of the thermonuclear plasmas produced through imaging of confinement events in real time have been a long-standing problem in the physics field. There

are three major methods used for confinement fusion: gravitational confinement, magnetic confinement, and inertial confinement [2]. Gravitational confinement fusion is typically only feasible at large scales and masses and is not able to be replicated on Earth due to the weakness of the confining force of gravity. Magnetic confinement fusion employs magnetic fields to enable fusion but has yet to achieve breakeven [1]. Out of the three methods, ICF is one of the most promising processes used for starting thermonuclear fusion through laserdriven implosion and was responsible for the achievement of scientific breakeven at the Lawrence Livermore National Laboratory's NIF [1]. Most commonly, ICF uses deuteriumdeuterium (DD) or deuterium-tritium (DT) fusion. It can be designed with direct or indirect drive [3,4]. Direct drive relies on multiple lasers directly energizing a small capsule of fuel, while indirect drive deposits this energy into a hohlraum around the capsule; in both cases the resulting heat and compression cause the capsule to implode and ablate [1,5].

The growing number of successful shots at NIF have necessitated new analysis approaches for ICF neutron imaging results¹. Pinhole and penumbral apertures are two of the most common methods employed for focusing neutrons enroute to a detector during the process of imaging ICF events [5]. Typically, pinhole apertures are smaller in size than the source while penumbral apertures are larger than the source. Both imaging approaches usually require the same type of image processing and reconstruction techniques to produce effective results [5]. This occurs because information captured during the ICF event is primarily found within the penumbral shadow of the aperture, which is more diffuse and indirect. In contrast, pinhole apertures provide a clearer, more direct image of the source. In this study, the NIF images used for denoising analysis were captured from plates that collected neutrons passing through straight pinhole apertures.

While pinhole imaging has many advantages when compared to neutron imaging from other apertures, certain challenges to visual data quality remain [6]. The low solid angle of pinhole apertures limits their ability to image certain smaller ICF cases appropriately due to decreased signal strength and neutron concentration per pinhole [5]. Additionally, pinhole images are more susceptible to noise when compared to annular or ring apertures [5]. Particularly in high-yield neutron shots, there are numerous sources of noise [4]. Poisson shot noise is produced due to discrete photons or particles colliding with the detector and is commonly present in low-light and low-yield conditions. Poisson noise becomes Gaussian when the photon

and particle count generated by the ICF event is higher than average due to the presence of electronic sensor noise. Uniform noise, much like Poisson noise, is seen in situations where lighting is poor. Salt-and-pepper noise arises during transmission errors or because of sensor defects. Finally, defects or scratches present on the plate or detector can directly affect the image, causing visible artifacts in those areas.

While there are a wide variety of noise combinations possible, in the case of the lower-yield shots used in this study, image analysis led to the conclusion that Poisson noise, Gaussian noise, and plate defects are the most common sources of noise to be addressed. After different particle conversions, gain stages, and background subtractions, the noise is closer to Gaussian noise than Poisson or combined Gaussian-Poisson noise in certain NIF images [5]. However, in low energy ICF pinhole shots, Poisson shot noise often combines with Gaussian and is the predominant source of noise in some images [5]. This necessitates extensive work in denoising pinhole images while still retaining the basic properties of the original image, with a specific focus on tackling edge preservation and source reconstruction for NIF data outputs.

Currently, ICF images are usually denoised via filtering methods such as Gaussian filtering, Wiener filtering, and BM3D [7,8]. In recent years, there has been an uptick in the usage of Convolutional Neural Networks (CNNs) to denoise real and simulated neutron pinhole images [9]. While unsupervised methods have been explored more frequently in the recent past due to their small-training-set robustness, they have not been popular for denoising ICF images due to the complex noise environment [10].

The current lack of ground truth data in ICF neutron imaging stems from two main factors. Firstly, there is a relatively limited body of experimental data from NIF, making it difficult to train and test large machine learning models. Additionally, there is a lack of noiseless, clean images that training sets can utilize to learn patterns. Because optimal supervised models must use simulated data conservatively in tandem with real-world data to gain accurate results, this necessitates the development and validation of unsupervised testing methods [8]. Methodologies such as clustering and unsupervised autoencoders can better leverage inherent features of the noisy images rather than relying on potentially inaccurate simulated ground truth datasets during training. Additionally, unsupervised networks require fewer simulated datasets posttuning, and less validation compared to supervised networks. While unsupervised machine learning methodologies have their own unique challenges with reconstruction error, a combination of an unsupervised method with a filtering method has not been significantly explored as an alternative. A literature search only yielded one study on this, where a fast Fourier transform was employed as a custom layer in a CNN [11]. This publication explores the use of an unsupervised denoising autoencoder with a discrete CDF 97 wavelet transform in the latent space to denoise and sharpen neutron pinhole images. The CDF 9/7 biorthogonal wavelet transform has been shown to be highly effective for image denoising due to its excellent energy compaction and smooth basis functions, which enable efficient separation of signal and noise components [12]. Model effectiveness was benchmarked using synthetic ground truth

data created by a forward model which was then corrupted by Gaussian and Gaussian-Poisson noise. The noise models produced results representative of experimental NIF data under different neutron yields. The model's performance relative to this synthetically generated ground truth was then compared with a regular autoencoder as a denoising strategy in addition to major filtering methodologies such as BM3D, Gaussian filtering, and Wiener filters; the model was able to outperform ML-only and filtering-only methods for edge preservation metrics such as polar and cartesian coordinate visualization, radial position of the edge, spread of the edge at transitions, residuals, and radial profile. Tikhonov regularization was also applied to evaluate how effectively the reconstruction recovered the original source.

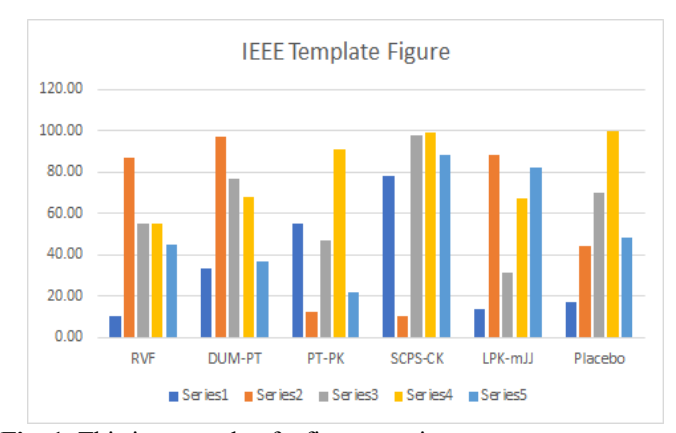


Fig. 1. This is a sample of a figure caption.

II. MATERIALS AND METHODS

An unsupervised autoencoder with custom layers in the latent space was utilized to denoise pinhole and penumbral data from the NIF dataset. Its performance was assessed using a forward model representing a neutron image. Through the images generated by a basic simulation, the quality of the simulated ground truth was assessed through various edge preservation metrics.

Three classes of datasets were used to validate the functionality of the autoencoder. The first one contained NIF data taken from neutron imaging plates captured by a camera during shots at the facility, while the last two contained data simulated using a forward model following a nonlinear Gaussian and Gaussian-Poisson noise model, respectively.

The NIF experimental data was taken from 2 plates captured from shot N210808 as shown in Figure 1 below.

Each plate had 64 pinholes each yielding a total available dataset of 128 images. The plate data was then split into smaller



Figure 1: Depiction of the neutron radiation emitted by the N210808 shot at a certain point in time. Neutrons produced during fusion are uncharged and highly penetrative, allowing them to travel to a scintillator, where they interact and generate visible light. On the left is an example of a pinhole image (top left) and penumbral image (bottom left). Samples for the autoencoder model were taken through region of interest (ROI) extraction of individual penumbra and pinholes.

regions of interest (ROIs) of size (256, 256) pixels to be passed through the autoencoder as separate datapoints. This dataset was used to prototype the preliminary autoencoder model and served as proof of concept for the feasibility of denoising work using machine learning methods.

The benchmarking datasets used for validating autoencoder functionality were simulated through a forward model that generated a noiseless, simulated ground truth sample of a pinhole or penumbral image. As demonstrated in Figure 2a, the model consisted of two key elements convolved together to produce the simulated ground truth. The Gaussian blur simulates a source image, while the disc represents a pinhole or penumbral aperture depending on its size. To simulate a pinhole, the disc was made to be smaller than the source image. To simulate a penumbral image, the disc was made larger than the source image.

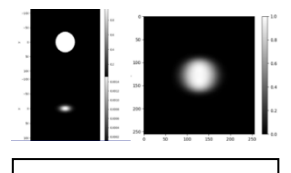


Figure 2a: Illustration of the forward model used for benchmarking. This setup was employed to simulate a penumbral image, which served as the central focus of the study. The simulated pinhole (top left) was convolved with the modeled source distribution (bottom left) to generate a simulated ground truth image of the penumbral aperture (right).

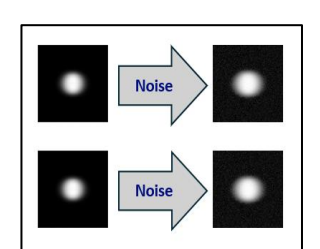


Figure 2b: A sample from the forward model image from Figure 2a with Gaussian noise (top) and mixed Gaussian-Poisson noise (bottom) added.

Two datasets representing the noise commonly seen in neutron shots were generated from the forward model. One dataset had exclusively signal-dependent Gaussian noise added to 3000 images, a sample of which is shown at the top of Figure 2a. For this noise model, ε represents Gaussian noise with a variance of 1:

$$I_{\text{noisy}} = I_{clean} + (RMS(I_{clean}) \times \varepsilon)$$

The other had a combination of Gaussian and Poisson noise as shown in the bottom image of Figure 2a as follows. The SNR is 10 and ε is Gaussian noise with the same parameters as the previous model.

$$I_{noisy}(x, y) = \frac{Poisson\left(\frac{SNR^2 * I_{noisy}(x, y)}{\max(I_{noisy})}\right) * \max(I_{clean})}{SNR}$$

The autoencoder was built using the PyTorch library and consists of 3 main components: an encoder, a linear transformation layer in the case of penumbral image denoising, a custom CDF 97 discrete wavelet transform layer, and a decoder. As shown in figure 3, the image undergoes a series of dimensional transformations as it propagates through the layers of the deep learning model.

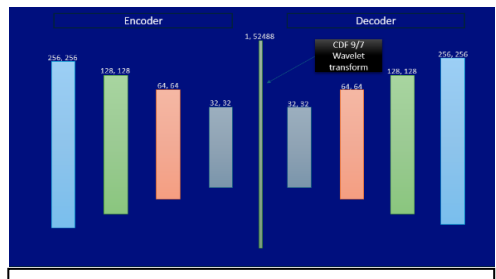


Figure 3: An illustration of the dimensional transformations applied to each image as it passes through the stages of the autoencoder. The repeated minimization of dimensions within the encoder portion allows for the identification and preservation of key features and the removal of noise vectors. The decoder is then able to reconstruct the denoised image using the most dominant features, while the CDF 9-7 wavelet transform removes any noise that was missed during the encoding and flattening process.

The encoder extracts the most relevant features from the inputs by down sampling each image individually. This down sampling process consists of six two-dimensional convolutional layers, each accompanied by leaky ReLU activation function layers that introduce non-linearity during training. This allows the model to learn image features more effectively when compared to linear processes such as Gaussian and Weiner filtering [13]. Meanwhile, the convolutional layers reduce the spatial resolution of the input image by half each time with a kernel size of 5x5, a stride of 2, and a padding value of 2. This combination of kernel size, stride, and padding results in reduction of image dimensions while maintaining the number of feature maps at each layer to ensure that the autoencoder has plenty of information to learn from during instantiation. The first and second convolutional layers were followed by pooling layers after the activation function. The third, fifth, and sixth convolutional and leaky ReLU function pairs were followed by a dropout layer. The fourth convolutional layer was followed by a dropout layer and pooling layer. Dropout layers were set to 0.2. They were utilized to help prevent overfitting by randomly zeroing twenty percent of the input units at each layer during each forward pass in the training loop (Srivastava). The pooling layers used had a window size of 2x2 and worked to reduce spatial dimensions even further to ensure that the image was of an appropriate size for the latent space to handle [14].

The encoded transformation is then passed through a custom transformation layer that applies a CDF 97 discrete

wavelet transform typically used for preserving image fidelity when compressing JPEG images [15]. In the case of penumbral images, a linear transformation is also applied. Mathematically, the CDF97 transform takes the following general form:

$$\tilde{f} = IDWT^L(DWT^L(f)) \approx f$$

L stands for the number of times the transform and its inverse are applied to the image in the latent space. The optimal number of levels was found to be 2, with further levels yielding diminishing returns for results. IDWT refers to the inverse wavelet transform, which is usually applied after performing a discrete wavelet transform (DWT) on an array.

All the synthesis and analysis filter coefficient arrays were initialized as 9-tap filters like so:

$$h[n] = \{h_0, h_1, h_2, h_3, h_4, h_5, h_6, h_7, h_8\}$$

However, the analysis high pass and synthesis lowpass filters were padded by zero at the 0th and 8th positions to replicate appropriate CDF97 behavior as described in the original Daubechies publication. The analysis low-pass and synthesis high-pass filters, on the other hand, are not padded and contain all 9 taps like so:

$$h[n] = \{h_0, h_1, h_2, h_3, h_4, h_5, h_6, h_7, h_8\}$$

$$h[n] = \{0, h_1, h_2, h_3, h_4, h_5, h_6, h_7, 0\}$$

This aligns with the boundary handling method described in the original implementation of the CDF 9/7 biorthogonal wavelet filter [12,16]. The numerical values of the nonzero coefficients were derived using the lifting scheme and scaling normalization steps developed by Daubechies [12]. When a linear transformation is needed, the image goes through the following changes in the latent space before being passed to the CDF97 wavelet transform:

$$y_{b,c,1,1} = \frac{1}{H \times W} \sum_{i=1}^{H} \sum_{j=1}^{W} x_{b,c,i,j}$$
$$x_{b,c,1,1} \to x_{b,c}$$
$$z_b = W x_b + b$$
$$y'_b = W' z_b + b'$$

These transformations stabilize the variance and reduce the impact of noise in image data. Moreover, the latent space keeps the image vectors (32, 32) in dimension. The feature maps stay constant as well.

After the images are passed through the latent space, the decoder reconstructs the original image from the representation passed to it from the custom layer. It consists of seven convolutional layers. The first two are followed by a batch normalization and leaky ReLU layer. The third and fourth layers are only superseded by leaky ReLU activation functions. To prevent checkerboarding in the image background during reconstruction, the last three layers are preceded by up-

sampling layers in bicubic mode. Each time, the image is upsampled by a factor of 2 using bicubic interpolation, which doubles the spatial dimensions at each step and reverses the down-sampling done by the encoder. While the first five activation layers are ReLU functions, the activation function of the last layer is a Sigmoid outputting values between 0 and 1. This makes it optimal for reconstructing and working with grayscale images that typically have pixel values between 0 and 1

The images were run through the autoencoder for 30 epochs. The learning rate was 0.001 and data indices were shuffled each epoch. A batch size of 10% of the sample size was found to be the most optimal for reconstruction. Hence, for the simulated ground truth data used for benchmarking, the batch size was set to be 300 and for the NIF data, the batch size was set to be 12. A smooth variant of the L1 loss, known as Smooth L1 or Huber loss, was used as the loss function. It behaves quadratically for small errors and linearly for large errors, reducing sensitivity to outliers while maintaining differentiability [17]. Smooth L1 Loss can be expressed mathematically like so:

$$L(x) = \begin{cases} 0.5(x - y)^2 & \text{if } |x - y| \le 0\\ |x - y| & \text{otherwise} \end{cases}$$

was used in lieu of Mean Squared Error due to its resilience to outliers and frequent use in image denoising and dehazing algorithms [18]. Additionally, when reconstruction error was compared, the model performed better with Smooth L1 Loss as opposed to MSE for the given datasets.

III. RESULTS

Both the synthetic ground truth and NIF datasets were utilized to generate and analyze results. These datasets objectively assessed the autoencoder's ability to denoise mixed Gaussian-Poisson noise under the physics constraints imposed upon the system by the forward model. The NIF dataset was used as proof of concept to ascertain that a basic autoencoder could perform generalizable denoising in practical, noisy conditions that reflect true experimental variability and Gaussian-Poisson characteristics within NIF datasets. The denoised, reconstructed results from the autoencoder were compared to datasets denoised with BM3D, a widely regarded benchmark method in image denoising [19]. For each method, the denoised reconstructions were compared to the ground truth. Assessment metrics included visual polar and cartesian coordinate visualization, radial position of the edge, spread of the edge at transitions, residuals, and radial profile. Tikhonov regularization, also known as ridge regression, was also applied along with Weiner deconvolution to evaluate how effectively the reconstruction recovered the original source when compared to the ground truth.

To create a reliable denoising solution for the images at hand, it was essential to validate that the noise present in the NIF data was indeed mixed Gaussian-Poisson in nature [5]. As an alternative, histogram analysis, local variance analysis, and power spectrum analysis as displayed in Figure 4 were

employed to acquire more information about the nature of the noise present in the data [20].

The results of these analyses for both pinhole and penumbral images indicate mixed Gaussian-Poisson noise. Pixel intensity histograms of NIF data are slightly skewed left with a bell-curve shape in both cases. This shape suggests the presence of

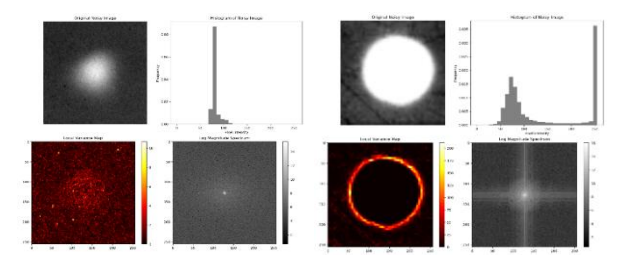


Figure 4: To confirm the type of noise present in the images, a histogram, local variance plot, and power spectra were generated for a pinhole and penumbral image from the N210808 shot. The noise was ascertained to be mixed Gaussian and Poisson across the images due to the features and characteristics of the plots.

Gaussian noise, while the skew indicates that Poisson noise may also contribute to visual distortions in the image [20]. In the case of the pinhole image, the local variance map displays higher variance in lighter areas of the image when compared to darker areas. A similar trend is seen at the edges of the penumbral image. Poisson noise in low-light conditions is often characterized as greater in magnitude at higher pixel intensities; hence, increased variance at higher pixel intensities in both images is an indicator of this type of noise [21]. In the case of the pinhole image, Fourier spectrum analysis results in a grainy background with poorly defined frequency and phase components. The background indicates that the image contains high levels of Gaussian noise, while the lack of frequency and phase bands in the case of the pinhole aperture indicate the presence of Poisson noise as well due to its signal dependent nature [22,23]. The pinhole, on the other hand, displays strong frequency and phase components against a grainy background. This indicates that while Poisson noise may not be as significant a problem in penumbral images, Gaussian noise is still pervasive throughout this portion of the image.

Reconstruction error measures the discrepancy between an autoencoder's input and its reconstructed output, often quantified using pixel-wise losses and structural similarity metrics. During training, the model's weights and biases are iteratively updated to minimize this error [24]. A viable autoencoder, in reconstructing noisy data, must be able to produce a result that matches the original ground truth image the inputs are derived from as closely as possible. While the most common method for assessing reconstruction fidelity is Mean Squared Error (MSE), other values such as Peak Signal to Noise Ratio, Structural Similarity Index, and edge preservation metrics [24,25]. Since the most significant aspect of reconstruction for neutron imaging is edge preservation and source reconstruction, most of the results are focused on this. Visual polar and cartesian coordinate visualization, radial position of the edge, spread of the edge at transitions, residuals, and radial profile were all considered. Additionally, Tikhonov regularization was also applied to

evaluate how effectively the reconstruction recovered the original source.

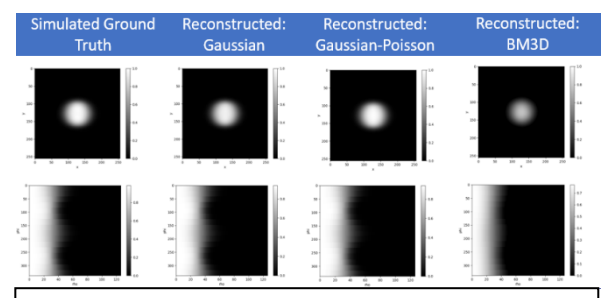
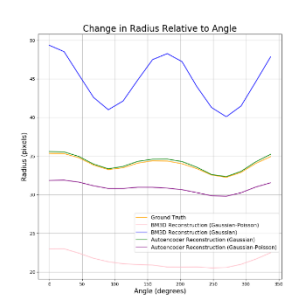
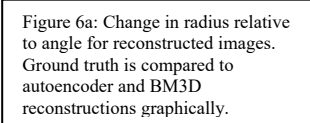


Figure 5: The simulated ground truth visualized side-by-side with autoencoder reconstructions of images corrupted by Gaussian noise and Gaussian-Poisson noise. For comparison, the BM3D method was utilized to reconstruct an image with Gaussian-Poisson noise and can be seen on the right. Both cartesian (top) and polar (bottom) results indicate higher fidelity between the ground truth and autoencoder reconstructions than compared to the ground truth and BM3D reconstruction.

Figure 5 displays a polar and cartesian visualization of the reconstructions indicated high fidelity between the ground truth and the denoised images. Key structural features and spatial patterns were preserved across both representations, indicating that the denoising process maintained the essential image characteristics without introducing noticeable artifacts. The alignment between the ground truth and denoised images was particularly evident in the preservation of the Gaussian blur along the edges. This suggests that the autoencoder effectively distinguishes between the blur inherent to the ground truth and extraneous noise introduced during noise generation in both the Gaussian and Gaussian-Poisson experimental cases. This selective retention further supports the qualitative accuracy of the reconstruction.





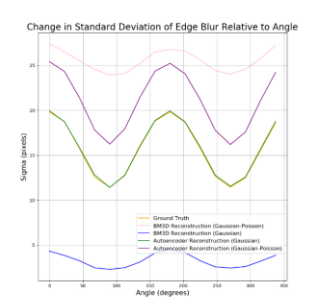


Figure 6b: Change in standard deviation of image edge blur in pixels relative to angle. Ground truth is compared to autoencoder and BM3D reconstructions graphically.

Figure 6a illustrates a quantitative analysis of the radius as a function of degree in the simulated ground truth, compared to autoencoder-based reconstructions under Gaussian and Gaussian-Poisson noise models, demonstrated performance on par with established denoising techniques such as BM3D. In images corrupted by Gaussian noise, the autoencoder reconstructions exhibited near-perfect agreement with the ground truth, accurately recovering the underlying magnitude of the radial profile. In the presence of Gaussian-Poisson noise, the reconstructions displayed a marginal

reduction in estimated radius of approximately four pixels but effectively preserved the overall radial trend consistent with the simulated ground truth. To further compare edge fidelity across differing denoising methods and noise models, the absolute radius error and relative fidelity scores were computed like so:

$$arepsilon_r = |\hat{r} - r_{GT}|$$
 $Fidelity_{AE\ vs.BM3D} = (1 - rac{arepsilon_r^{AE}}{arepsilon_r^{BM3D}}) imes 100$

For samples corrupted by Gaussian noise, the autoencoder reconstructions showed a mean absolute radius error of pixels, outperforming BM3D's pixels. The relative fidelity scores were computed to be ____ % and ____ %, respectively. For samples corrupted by Gaussian-Poisson noise, autoencoder reconstructions showed a mean absolute radius error of pixels, while BM3D reconstructions had an error of pixels. For these sample sets, the relative fidelity scores were % for autoencoder reconstructions and % for BM3D reconstructions. Additionally, the Pearson correlation coefficient was computed for radial profiles to assess structural fidelity. Under Gaussian noise, the autoencoder achieved a correlation of ____, slightly higher than BM3D's ____. Under Gaussian-Poisson noise, all methods exhibited decreased correlation of _____, with the autoencoder maintaining strong agreement around____. These results demonstrate that the autoencoder preserves radial structure with high accuracy under both noise models and performs competitively with traditional denoising methods, particularly in terms of structural and metric fidelity.

Figure 6b above shows a visualization of the Gaussian blur variance, also known as σ at edge transitions in the reconstructions exhibited high fidelity to the ground truth in images degraded by Gaussian noise, accurately preserving edge sharpness and gradient continuity. This is supported by a high edge PSNR of 34.2 dB and a low gradient magnitude similarity deviation (GMSD) of 0.078. Under Gaussian-Poisson noise, the reconstructions exhibited elevated variance levels, reflecting the autoencoder's increased difficulty in disentangling structured blur from unnecessary noise under more complex noise conditions. This is supported by an elevated local gradient variance at the edges, rising from _____ to ____. Despite this challenge, the reconstructions maintained the expected σ-blur trend, albeit at a higher variance overall. Autoencoder-based methods outperformed BM3D in preserving the integrity of the σ profile in both Gaussian and Gaussian-Poisson noise situations, demonstrating superior retention of spatially dependent blur characteristics when compared to conventional filtering methods. Specifically, the mean squared error (MSE) between the reconstructed and ground truth σ -blur profiles was for the autoencoder, compared to for BM3D. indicating significantly improved spatial fidelity in blur retention. Additionally, edge PSNR and GMSD scores consistently favored the autoencoder, underscoring its superior ability to preserve spatially dependent blur characteristics compared to conventional filtering approaches.

Figure 7 displays residual analysis of the reconstructions relative to the ground truth. It demonstrated high fidelity in the presence of Gaussian noise. Residuals in this

case were tightly distributed, with a mean of 0.012, a median of 0.011, and a standard deviation of 0.005. Residual values were consistently constrained within the range [0.00, 0.03] across the image domain. For images affected by Gaussian-Poisson noise, residuals were notably higher and more dispersed, with a mean of 0.041, a median of 0.038, and a standard deviation of 0.018. They generally ranged between [0.00, 0.10], reflecting the increased complexity in accurately reconstructing pixel intensities under mixed noise conditions. However, the autoencoder was able to reduce residuals of the reconstructions by 71.4% on average in the case of images corrupted by Gaussian-Poisson noise and by 70.0% on average in the case of images corrupted by Gaussian noise alone. This is an improvement when compared to BM3D, which only reduces residuals by % on average in the case of images with % in the case of images with Gaussian-Poisson noise and

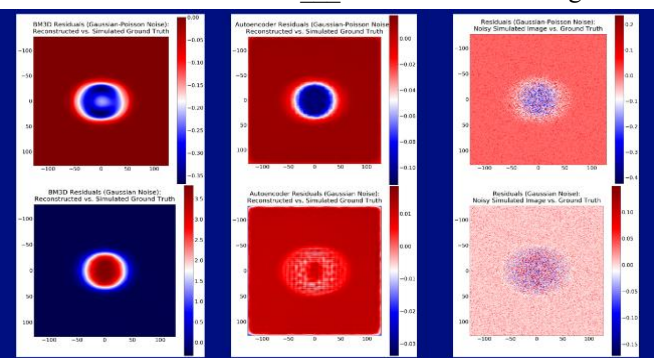
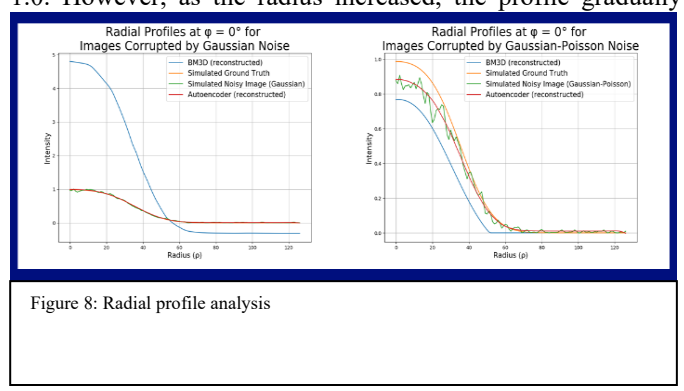


Figure 7: Residual analysis of reconstructions relative to the ground truth indicates high fidelity in the presence of Gaussian noise. Autoencoder reconstructions outperformed BM3D reconstructions in the presence of mixed Gaussian-Poisson noise.

Gaussian noise alone. In the case of BM3D, the average residual values of 0.059 (mean), 0.055 (median), and 0.022 (standard deviation) under Gaussian-Poisson noise, and 0.021 (mean), 0.020 (median), and 0.007 (standard deviation) for Gaussian noise demonstrate the autoencoder's improved denoising capability when compared to BM3D in the presence of complex, nonlinear noise.

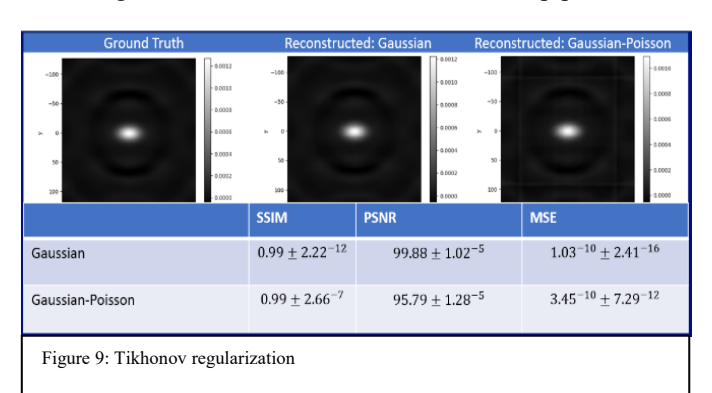
As shown in figure 8 below, radial profile analysis of the autoencoder reconstructions relative to the simulated ground truth revealed that, under Gaussian-Poisson noise, the reconstructed pixel intensities were initially attenuated, with values starting around 0.8 compared to the ground truth peak of 1.0. However, as the radius increased, the profile gradually



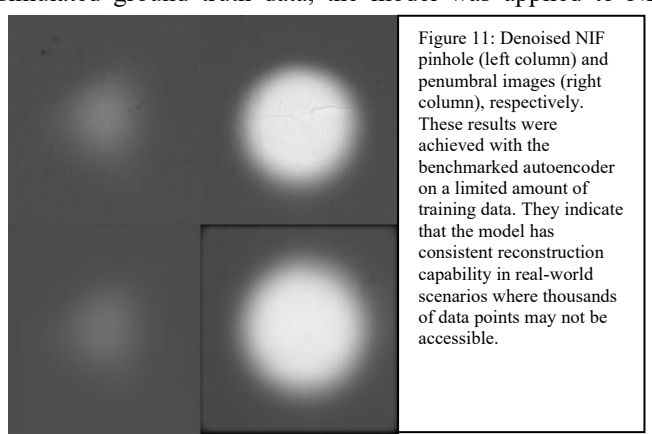
converged toward the ground truth, indicating that the reconstruction effectively recovered the overall structure despite initial underestimation. In contrast, reconstructions

from Gaussian noise exhibited near-perfect alignment with the ground truth across the entire radial domain, demonstrating the autoencoder's high fidelity under simpler noise conditions.

To validate the fidelity of the reconstructions further, the source image was recovered from both the ground truth and reconstructed outputs using Wiener deconvolution in conjunction with Tikhonov regularization, incorporating the known point spread function (PSF) of the forward model defined as the sum of the initial disc before convolution with the source of the forward model. In both the Gaussian and Gaussian-Poisson noise scenarios, the deconvolved reconstructions closely approximated the true source, demonstrating the autoencoder's ability to preserve critical spatial information through the noise. The recovered sources exhibited high structural similarity to the ground truth, further validating the effectiveness of the reconstruction pipeline under



varying noise conditions. Figure 9 shows a visualization of the results relative to the ground truth along with structural similarity, peak signal to noise ratios, and mean squared error values. After training and validating the autoencoder using simulated ground truth data, the model was applied to NIF



pinhole and penumbral images. Figure 10 displays the results of running the autoencoder on 50 pinhole images and 6 penumbral images with a batch size of 6 and 2, respectively. The reconstructions exhibited strong qualitative and quantitative agreement with expected structural features, indicating that the autoencoder successfully generalized from simulated to real-world conditions. This demonstrates the model's robustness and practical applicability in processing experimental data following tuning on synthetic datasets.

IV. DISCUSSION

Our study found that an unsupervised machine learning approach outperforms conventional methods when reconstructing images corrupted with Gaussian and Gaussian-Poisson noise in physics models. The observed improvements in reconstruction quality and edge preservation suggest that unsupervised learning frameworks offer a viable and scalable alternative in the denoising work necessary to optimize operations in computational physics. These methods can autonomously learn from intrinsic data features, reducing reliance on external training datasets and potentially simplifying implementation across diverse noise models. Results indicate that an unsupervised autoencoder model is particularly effective in preserving image edges when reconstructing samples corrupted by Gaussian noise.

For images affected by Gaussian-Poisson noise, the model achieved performance comparable to conventional methods. Most prior studies in image reconstruction of samples corrupted by Gaussian and Gaussian-Poisson noise in ICF imaging have relied on supervised learning frameworks which require large, labeled training datasets [5]. In contrast, this work's unsupervised autoencoder approach operates without external labels and learns directly from the noisy input data. While supervised models have achieved strong results, unsupervised models have the potential for superior performance in edge preservation under Gaussian and Gaussian-Poisson noise above that of conventional methods, a particularly important metric to address in physics contexts where low-noise ground truth data is unavailable. Unsupervised frameworks can therefore provide viable, data-efficient alternatives that more closely match reality.

These results underscore the utility of unsupervised learning as a powerful tool in denoising neutron imaging data for ICF research. The autoencoder framework presented here not only eliminates the need for large, labeled datasets but also reduces the complexity of preprocessing pipelines, such as multi-step transformations often used for Gaussian-Poisson denoising. This reduction in complexity is particularly valuable in high-throughput environments like the National Ignition Facility, where real-time or near-real-time image processing is advantageous for adjusting experimental parameters on the fly. Additionally, by incorporating a CDF 97 wavelet transform in the latent space, the network gains sensitivity to fine-grained features across multiple scales—an essential quality for detecting subtle spatial patterns and edge information in neutron source distributions. Wavelet-based representations appear to complement and enhance the autoencoder's ability to generalize, offering a more robust encoding of structural features that conventional filtering methods tend to degrade.

V. CONCLUSION

This study demonstrates the effectiveness of using an unsupervised autoencoder constructed with custom and convolutional layers for the denoising of NIF ICF pinhole images. This method outperforms widely utilized filtering methods such as BM3D, Wiener filtering, and Gaussian filtering when minimizing reconstruction error and maximizing edge preservation. Additionally, it decreases the reliance of the

model on simulated data past validation of its efficacy when compared to supervised machine learning denoising methods that always require a training set that often needs to be simulated due to a lack of ground truth data. The custom layer in the bottleneck of the autoencoder contributes to better denoising performance when compared to baseline models without it. Improving unsupervised denoising methods is essential for better visualizing ICF events, as a lot of images are taken in low-light conditions where it is difficult to find a ground truth or even have a large training set of real data. Autoencoders perform denoising by relying solely on features extracted directly from the input image, rather than external training datasets. often rely solely on the image itself during denoising, with the denoising process being based on key features extracted from the image currently being processed by the autoencoder. It is directly informed by the key features of the image at hand as opposed to arbitrary or simulated ground truth training datasets. Unsupervised methods are more adaptable to real-world scenarios like ICF, where acquiring ground truth experimentally is not feasible. However, it is imperative to quantify overfitting and ensure that the boundaries for the algorithm's utility are established. Future work would involve addressing the limitations of the current methodology. Currently, the model has primarily been tested on neutron images and has not been validated to be generalizable to other types of images such as x-ray images. It has also not been rigorously validated with various source shapes and apertures that are utilized less often. Additionally, the model is not generalized to large pixel spaces and the images being fed into it are currently just smaller segments of a wider neutron imaging plate. Finally, despite its strengths, limitations remain in the unsupervised model's ability to fully resolve nonlinearities introduced by compound noise distributions such as overlapping Poisson-Gaussian processes. Future work should explore the integration of physics-informed loss functions or hybrid models that combine unsupervised and semi-supervised paradigms to further improve noise-specific adaptability. Exploring domain-specific augmentations or incorporating simulation-based priors may also enhance model performance, particularly in low-signal or anisotropic imaging scenarios typical of early-stage ICF implosions. Ultimately, the findings from this study reinforce the potential of unsupervised machine learning for neutron image enhancement and open the door to a broader class of self-tuning algorithms for ICF diagnostics. By bridging the gap between traditional filtering approaches and data-intensive supervised learning, methodology presents a proof-of-concept for a scalable, generalizable framework for future fusion research applications, including time-series denoising, 3D tomographic reconstruction, and anomaly detection in neutron yield patterns. In a field where ground truth is not easily available, the applicability of unsupervised methods in this space is explored though this study.

REFERENCES

[1] O. Hurricane, P. Patel, R. Betti, D. Froula, S. Regan, S. Slutz, M. Gomez, and M. Sweeny, "Physics principles of inertial confinement fusion and U.S. program overview," *Reviews of Modern Physics*, vol. 95, Jun. 2023, doi: https://doi.org/10.1103/RevModPhys.95.025005

- [2] D. Keefe, "Inertial Confinement Fusion," Lawrence Berkeley National Laboratory, LBNL Report #: LBL-14194, Mar. 1982.
- [3] Z. Lu, S. Jia, G. Li, and S. Jing, "Neutron image denoising method based on adaptive new wavelet threshold function," *Nuclear Instruments and Methods in Physics Research Section A Accelerators Spectrometers Detectors and Associated Equipment*, vol. 1059, pp. 169006–169006, Dec. 2023, doi: https://doi.org/10.1016/j.nima.2023.169006.
- [4] Naima Naheed, B. T. Wolfe, and Z. Wang, "Noise classification of ICF images using a convolutional neural network (CNN)," Zenodo (CERN European Organization for Nuclear Research), Aug. 2023, doi: https://doi.org/10.5281/zenodo.8368998.
- [5] D. N. Fittinghoff, N. Birge, and V. Geppert-Kleinrath, "Neutron imaging of inertial confinement fusion implosions," *Review of Scientific Instruments*, vol. 94, no. 2, Feb. 2023, doi: https://doi.org/10.1063/5.0124074.
- [6] H. Feng, L. Wang, X. Wang, and J. Jin, "Ultrasonic manipulation for precise positioning and equidistant transfer of inertial confinement fusion microspheres," *Ultrasonics*, vol. 126, p. 106806, Dec. 2022, doi: https://doi.org/10.1016/j.ultras.2022.106806.
- [7] B. T. Wolfe, P. Chu, N. Nguyen-Fotiadis, X. Zhang, M. A. Alvarez, and Z. Wang, "Machine learning-driven image synthesis and analysis applications for inertial confinement fusion (invited)," *Review of Scientific Instruments*, vol. 95, no. 12, Dec. 2024, doi: https://doi.org/10.1063/5.0219412.
- [8] Y. Xiaohui et al., "Image restoration method suitable for neutron imaging system image and based on Gauss-Poisson hybrid noise model," European Patent Office.
- [9] Z. Lu et al., "Neutron radiographic images denoising method based on multi-branch network," Nuclear Instruments and Methods in Physics Research Section B Beam Interactions with Materials and Atoms, vol. 553, pp. 165402–165402, May 2024, doi: https://doi.org/10.1016/j.nimb.2024.165402.
- [10] X. Lin, C. Ren, X. Liu, J. Huang, and Y. Lei, "Unsupervised Image Denoising in Real-World Scenarios via Self-Collaboration Parallel Generative Adversarial Branches," 2021 IEEE/CVF International Conference on Computer Vision (ICCV), pp. 12608–12618, Oct. 2023, doi: https://doi.org/10.1109/iccv51070.2023.01162.
- [11] X. Li et al., "FEUSNet: Fourier Embedded U-Shaped Network for Image Denoising," Entropy, vol. 25, no. 10, pp. 1418–1418, Oct. 2023, doi: https://doi.org/10.3390/e25101418.
- [12] I. Daubechies and Wim Sweldens, "Factoring wavelet transforms into lifting steps," *Journal of Fourier Analysis and Applications*, vol. 4, no. 3, pp. 247–269, May 1998, doi: https://doi.org/10.1007/bf02476026.
- [13] N. Kulathunga et al., "Effects of the Nonlinearity in Activation Functions on the Performance of Deep Learning Models," doi: https://doi.org/10.48550/arXiv.2010.07359
- [14] A. Krizhevsky, I. Sutskever, and G. E. Hinton, "ImageNet Classification with Deep Convolutional Neural Networks," *Communications of the ACM*, vol. 60, no. 6, pp. 84–90, May 2012.
- [15] J. Mishra and V. Kumar, "Study of Digital Image Compression Techniques and Framework for Suitability Selection based on Similarity Measuring Metrics," 2022 13th International Conference on Computing Communication and Networking Technologies (ICCCNT), pp. 1–6, Jun. 2024, doi: https://doi.org/10.1109/icccnt61001.2024.10724007.
- [16] J. Park, D. Kwon, Y. Song, and C. Ahn, "A Study on Feature Extraction of Transformers Aging Signal using Discrete Wavelet Transform Technique," *Proceedings of the Korean Institute of Electrical and Electronic Material Engineers Conference*, pp. 5-12, May. 2000.
- [17] C. Liu et al., "Adaptive Smooth L1 Loss: A Better Way to Regress Scene Texts with Extreme Aspect Ratios," 2021 IEEE Symposium on Computers and Communications (ISCC), Sep. 2021, doi: https://doi.org/10.1109/iscc53001.2021.9631466.
- [18] Zhu, Xinshan et al. "Multi-Stream Fusion Network With Generalized Smooth L1 Loss for Single Image Dehazing." *IEEE transactions on image processing* 30 (2021): 7620–7635. Print.
- [19] Ahmed, A. M. Jawad, S. A. Abdulkareem, F. M. Mustafa, Svitlana Ivanchenko, and Serhii Toliupa, "BM3D Denoising Algorithms for Medical Image," *DOAJ (DOAJ: Directory of Open Access Journals)*, pp. 135–141, Apr. 2024, doi: https://doi.org/10.23919/fruct61870.2024.10516419.
- [20] S. Akbar and A. Verma, "Analyzing Noise Models and Advanced Filtering Algorithms for Image Enhancement."
- [21] K. G. Lore, A. Akintayo, and S. Sarkar, "LLNet: A deep autoencoder approach to natural low-light image enhancement," *Pattern Recognition*,

> REPLACE THIS LINE WITH YOUR MANUSCRIPT ID NUMBER (DOUBLE-CLICK HERE TO EDIT) <

- vol. 61, pp. 650–662, Jan. 2017, doi: https://doi.org/10.1016/j.patcog.2016.06.008.
- [22] T. Le, R. Chartrand, and T. J. Asaki, "A Variational Approach to Reconstructing Images Corrupted by Poisson Noise," *Journal of Mathematical Imaging and Vision*, vol. 27, no. 3, pp. 257–263, Mar. 2007, doi: https://doi.org/10.1007/s10851-007-0652-y.
- [23] A. Faramarzi, A. Ahmadyfard, and H. Khosravi, "Adaptive Image Super-Resolution Algorithm Based on Fractional Fourier Transform," *Image Analysis & Stereology*, vol. 41, no. 2, pp. 133–144, Jul. 2022, doi: https://doi.org/10.5566/ias.2719.
- [24] F. Zhuang, Supervised Representation Learning: Transfer Learning with Deep Autoencoders
- [25] L. Gondara, "Medical Image Denoising Using Convolutional Denoising Autoencoders," *IEEE Xplore*, 2016. https://ieeexplore.ieee.org/abstract/document/7836672/
- [26] A. Bijaoui, E. Slezak, "Analysis of radial profiles," Jan. 1987.
- [27] C. Zucker and H. H.-H. Chen, "RadFil: A Python Package for Building and Fitting Radial Profiles for Interstellar Filaments," *The Astrophysical Journal*, vol. 864, no. 2, p. 152, Sep. 2018, doi: https://doi.org/10.3847/1538-4357/aad3b5.
- [28] E. Mavridaki and V. Mezaris, "NO-REFERENCE BLUR ASSESSMENT IN NATURAL IMAGES USING FOURIER TRANSFORM AND SPATIAL PYRAMIDS," in *IEEE Proceedings*, IEEE, Oct. 2014.